Optical Huygens' Metasurfaces with Independent Control of the Magnitude and Phase of the Local Reflection Coefficients

Minseok Kim, Alex M. H. Wong, and George V. Eleftheriades[*]

The Edward S. Rogers Department of Electrical and Computer Engineering,
University of Toronto, Toronto, Canada M5S 3G4
(Received 23 June 2014; published 9 December 2014)

Implementation of abrupt phase discontinuities along a surface has been the theme of recent research on electromagnetic metasurfaces. Simple functionalities such as reflecting, refracting, or focusing plane waves have been demonstrated with devices featuring phase discontinuities, but optical surfaces allowing independent magnitude and phase control on the scattered waves have yet to emerge. In this paper, we propose the first true optical Huygens' surface, which explicitly utilizes orthogonal electric and magnetic responses to realize total control on an optical surface's local reflection coefficients. This extends the functionality of metasurfaces to an unprecedented level. We first demonstrate that a nanorod gap-surface plasmon resonator can act as a Huygens' source. Thereafter, by properly tuning and rotating these resonators, we realize arbitrary reflection optical metasurfaces—surfaces for which the local reflection coefficients can be independently tailored in both magnitude and phase. We demonstrate the versatility of this approach through designs of a metasurface that asymmetrically reflects two copolarized beams and a Dolph-Tschebyscheff optical reflectarray.

I. INTRODUCTION

Much recent scientific activity surrounds the prospective realization of an ultimate electromagnetic (EM) surface that would allow full control on the reflective and transmissive properties of light. While practical implementations for holograms [1–3] and holographic antennas [4,5] allow one to perform a wide variety of wavefront manipulation, the drive to control an EM wavefront at the highest resolution and across the widest possible angle has led to the emergence of a new class of EM surfaces. In this effort, artificial surfaces have been demonstrated which systematically manipulate the reflection or transmission phase of an incident wavefront. In particular, Yu *et al.* [6–8] captured much attention with a proposal to modify the refraction phase of midinfrared EM waves using a surface of V-shaped nanoantennas. Subsequent works by Ni *et al.* led to first demonstrations of single-layer metasurfaces at near-infrared and optical frequencies [9], as well as demonstrations of similar properties for Babinet-inverted V-slot metasurfaces [10]. Notwithstanding, these single-layer metasurfaces suffer three major limitations: First, they do not allow independent control of the magnitude and phase of the surface's local transmission and/or reflection

coefficients; second, their cross-polarized operation leads to the existence of a spurious copolarized component which limits the achievable power efficiency to 25% [11], without accounting for material loss; last, they cannot support arbitrary field distributions on either side of the surfaces. Alternative structures have been proposed that adjust the phase of an optical wavefront through polarization manipulations. These Pancharatnam-Berry phase metasurfaces were demonstrated first in the midinfrared [12] then recently in the optical domain [13]. Using the Pancharatnam-Berry phase allows one to attain a full 360° phase shift with a single-layer electrical metasurface, as well as avoid the aforementioned limit on power efficiency. Nonetheless, the versatility of these metasurfaces is appreciably limited by (1) their inability to control the transmission or reflection magnitude and (2) their restriction to circular polarization operation.

In parallel to this work, Pfeiffer *et al.* [14] and Selvanayagam *et al.* [15] proposed metasurfaces that feature a subwavelength array of orthogonal electric and magnetic dipole elements. These so-called Huygens' surfaces mimic the emission of secondary wavelets as proposed in the Huygens' principle, and hence they allow one to assume total control on electromagnetic waves transmitted and reflected across a surface. Nonetheless, an optical implementation of such a surface is not at all straightforward. While Refs. [14] and [16] demonstrated Huygens' metasurfaces in the microwave regime, the same has not been accomplished in the optical regime, because of fabrication difficulties, the unavailability of lumped circuit

[*]gelefth@ece.utoronto.ca

elements, the plasmonic nature of metal, and a lack of suitable magnetic materials at optical frequencies. Instead, recent implementations of "Huygens' like" surfaces at optical and infrared frequencies have adopted a multilayered structure [17,18], for which it has been proven that electrical responses alone suffice to synthesize arbitrary reflection and transmission properties [11]. While such demonstrations represent the culmination of impressive theory and fabrication, multilayered subwavelength optical surfaces require layer-by-layer fabrication and precise alignment, and hence they are very complicated to fabricate. Moreover, they inevitably incur loss due to the plasmonic nature of metal. For example, the near-infrared Huygens' like surface described in Ref. [18] had a simulated power efficiency of 30%. This is decidedly lower than unity, even though it already represents about an order of magnitude improvement over most previously proposed optical metasurfaces. One would expect more stringent fabrication tolerances and dramatically higher losses for metasurfaces that operate at visible frequencies. Very recently, Estakhri *et al.* proposed a metasurface that featured a single layer of electrical response components, backed by a metallic mirror [19]. While this simplified multilayer device should theoretically improve efficiency, it fails to shape the amplitude of an impinging wave, similarly to aforementioned single-layered optical metasurfaces [6–10]. In view of shortcomings of all aforementioned proposals, implementing an optical Huygens' surface opens an ideal path towards attaining total control on optical wavefronts.

In this paper, we present the first true optical Huygens' metasurfaces and demonstrate their use for versatile arbitrary spatial light modulation at visible frequencies. Using an array of nanorods that is closely placed on a metallic layer, we achieve an optical Huygens' surface that allows one to independently tune the magnitude and phase of the surface's local reflection coefficients, with a magnitude range of [0, 0.67] and a full phase range of 360°. The simple device structure lends itself to relatively straightforward fabrication and low loss, with a simulated power efficiency of 45% for an operational wavelength of 800 nm—well beyond theoretical limits for metasurfaces that feature multilayered structures or cross-polarized operation. The above quoted power efficiency represents the power ratio of the reflected beam over the incident beam, taken in the "worst case" where all nanorods are tuned to maximize absorption and polarization loss. Hence, higher efficiency can be attained for selected waveform designs. We first describe our metasurface design procedure, which leverages a generalized equivalent circuit for Huygens' metasurfaces [20]. We point out that to achieve full control over the reflected light field, one needs a Huygens' metasurface with a user-designed spatially varying reflection loss (in addition to reactance), which has heretofore been neglected in metasurface design. We then describe our method for

synthesizing the required lossy and reactive metasurface using a rotated nanorod array that utilizes a gap-surface plasmon mode [21]. We show that one can systematically tune the reflection of such nanorod elements, in a way closely analogous to tuning the impedance of an electronic circuit through the use of "Smith Charts." Physical insights will be emphasized. Our procedures will be shown through a demonstration of a metasurface that asymmetrically reflects an incident plane wave into two copolarized plane waves, which, while simple, illustrates the procedure and highlights the need for synthesizing complex reflection coefficients. Finally, we close by connecting this work with the design and implementation of a Dolph-Tschebyscheff optical reflectarray—an array that redirects an incident beam at a prescribed direction with equal sidelobe amplitude and minimal beamwidth.

II. DESIGN CONCEPT AND NUMERICAL RESULTS

To first demonstrate how the independent tuning of the magnitude and phase of the local reflection coefficient broadens the functionality of the metasurfaces, we give an example of a beam splitter, shown in Fig. 1, where a normally incident beam at 800 nm is split into two copolarized reflection beams, reflecting at −15° and 45°, respectively. Though simple, this example demonstrates functionality that cannot be realized with surfaces that do not have any means of magnitude control and only provide abrupt phase discontinuities at a fixed scattering magnitude (which have been the subject of analysis in most previous works) because they do not satisfy the electromagnetic boundary conditions for the given stipulated fields. To illustrate this point, we first assume that our surface is formed with closely spaced, subwavelength-sized inclusions that possess both electric and magnetic polarizabilities. Electromagnetic radiation incident upon this surface would excite electric and magnetic dipoles, which can be homogenized as electric and magnetic currents, or
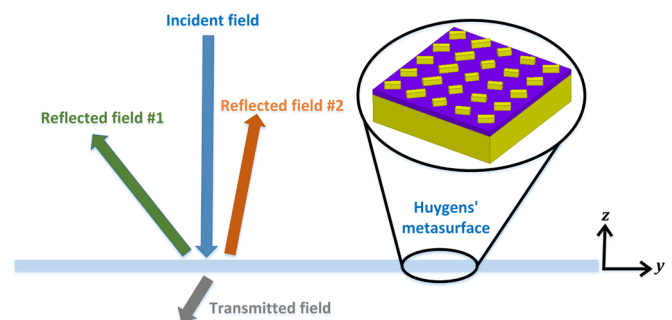

FIG. 1. Field distribution of a metasurface that asymmetrically reflects an incident plane wave into two copolarized plane waves. The incident plane wave is linearly polarized light along the *y* direction, and it propagates along the −*z* direction. The two reflected fields of the same polarization are split at −15° and 45°.

equivalently as electric and magnetic surface impedances denoted as Z_s^e and Z_s^m, respectively [14,22,23]. Such impedances are, in general, complex-valued tensorial quantities; however, in this work, we explore a space where they are isotropic and passive but will, in general, possess a user-designed polarization loss and reactance. As we show, this allows the surface to satisfy the boundary conditions for arbitrary copolarized field distributions on either side of the surface.

By denoting the net fields in two media separated by the surface as $\vec{E}_1$, $\vec{H}_1$ and $\vec{E}_2$, $\vec{H}_2$, the boundary conditions are given by [23]

$$\vec{E}|_{\text{avg}}^{\text{t}} = Z_s^e \vec{a}_n \times (\vec{H}_2 - \vec{H}_1), \quad (1)$$

$$\vec{H}|_{\text{avg}}^{\text{t}} = -(1/Z_s^m)\vec{a}_n \times (\vec{E}_2 - \vec{E}_1), \quad (2)$$

where $\vec{E}|_{\text{avg}}^{\text{t}}$ and $\vec{H}|_{\text{avg}}^{\text{t}}$ represent the average electric and magnetic fields tangential to the surface. For example, assuming the surface is located at $z = 0$, $\vec{E}|_{\text{avg}}^{\text{t}} = 1/2(\vec{E}_1^{\text{t}}|_{z=0^+} + \vec{E}_2^{\text{t}}|_{z=0^-})$. We stipulate the desired electromagnetic fields as design variables, then solve for the corresponding surface impedances using Eqs. (1) and (2). Moreover, to ensure that the surface remains passive, we design the two reflected beams so that each attains a field amplitude 41% that of the incident beam and a negligible transmitted field. Notwithstanding, the method can be generalized to study active metasurfaces, for which field amplitudes of reflected and transmitted beams can be arbitrarily stipulated.

Figures 2(a) and 2(b) show the distribution of the complex impedances along the surface that satisfy Eqs. (1) and (2). In these figures, the positive surface resistance (R_s^e and R_s^m) indicates that the surface remains passive. Clearly, both Z_s^e and Z_s^m must, in general, be complex valued; hence, purely reactive surfaces that only alter the phase of the scattered field cannot function as a beam splitter. It should further be noted that both Z_s^e and Z_s^m are aperiodic in the most general case. This is seen by noting that they are functions of spatial harmonics with arguments $\phi_0 = ky(\sin\theta_t - \sin\theta_i)$, $\phi_1 = ky(\sin\theta_{r1} - \sin\theta_i)$, and $\phi_2 = ky(\sin\theta_{r2} - \sin\theta_i)$, where k is the wave number and θ_{r1}, θ_{r2}, θ_t, and θ_i, respectively, represent the two reflection angles, the transmission angle, and the incidence angle. Hence, Z_s^e and Z_s^m are periodic only when the above arguments have common multiples.

In the following, we propose a physical structure of an inclusion that forms our surface and substantiate that it behaves like a Huygens' source. We then convert the complex surface impedances shown in Fig. 2 to their equivalent reflection coefficients by leveraging a circuit model for a Huygens' source. As we will show, one needs to independently control the magnitude and phase of the
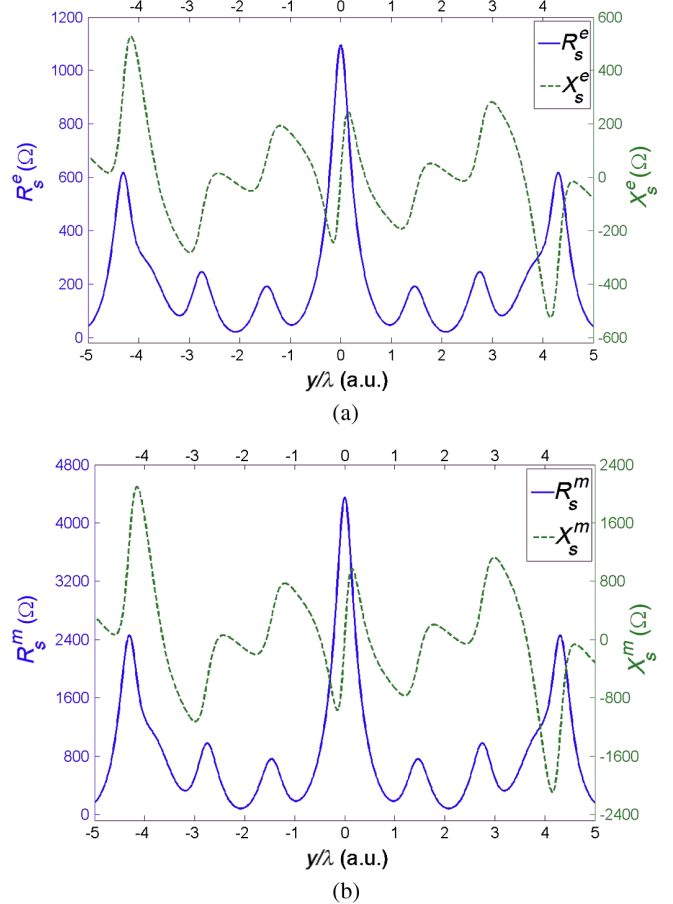

(a)

(b)

FIG. 2. The required (a) electric and (b) magnetic surface impedances that satisfy the boundary conditions for the field distribution shown in Fig. 1. R_s and X_s respectively represent the real and imaginary parts of the complex impedances.

local reflection coefficients to sample the equivalent reflection coefficient distribution. We will explain how the proposed physical structure can be properly tuned and rotated to achieve such a goal and thereby physically realize the current design example of a beam splitter.

A. Gap-surface plasmon resonator as a Huygens' source

To physically implement the required surface impedances, we utilize a nanorod gap-surface plasmon (GSP) resonator (shown in Fig. 3) as our unit cell to form the proposed metasurface. Before we demonstrate independent tuning of magnitude and phase of the reflection coefficient of such a unit cell for sampling the required surface impedances, we first establish that a nanorod GSP resonator indeed behaves like a Huygens' source. It consists of a gold nanorod (with thickness $t_1 = 50$ nm and width $w = 50$ nm) on top of a silica spacer (with thickness $t_2 = 50$ nm) and an optically thick gold layer. The periodicity of the unit cell is $d_x = d_y = 240$ nm. An optically thick gold layer is employed to simplify numerical
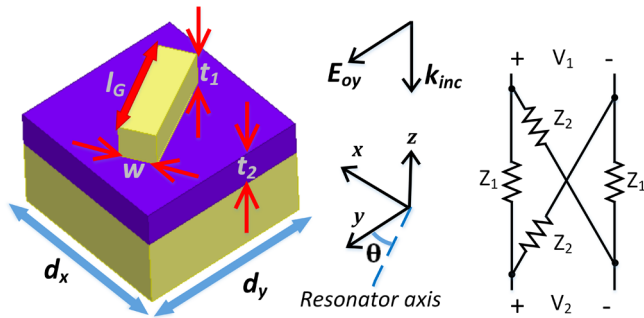
FIG. 3. The schematic of a nanorod GSP resonator unit cell that forms the Huygens' metasurface and the proposed equivalent circuit model.

(a)

(b)

simulations; however, an almost identical optical response can be obtained with a gold layer of subwavelength thickness (around 100 nm). Hence, the overall thickness of the GSP resonator is still subwavelength. The proposed configuration has been extensively studied in the past for its use in biosensors [24–27] and metasurface designs [21,28–30]. Previous analyses, however, have focused on the plasmonic mode properties of the structure perceived as a nanorod metasurface placed close to a metallic back reflector. On the contrary, we view the combination of nanorods, dielectric spacer, and back metal as a single-layered metasurface where each unit cell functions analogously to a Huygens' source.

In essence, the nanorod and the metallic substrate act as a Fabry-Perot resonator that supports two dominant modes: one that features symmetric current flow, leading to an effective electric dipole, and another that features asymmetric current flow, leading to an effective magnetic dipole [21]. We note that these induced dipoles are orthogonal to each other in the plane of the metasurface and that they closely resemble Huygens' sources—the fundamental building block for reshaping a reflected wavefront. An ideal Huygens' source features orthogonal electric and magnetic currents that radiate in phase and in equal power. Such a source generates a unidirectional far-field radiation pattern with a maximum directivity of 3 [31–33]. Figure 4(a) shows the radiation pattern of a single isolated unit cell that is electromagnetically similar to the nanorod GSP resonator. The observed cardioid radiation pattern is similar to that of a Huygens' antenna [34,35] and demonstrates (i) the simultaneous existence of electric and magnetic dipoles and (ii) their orthogonal directional relationship. As a comparison, Fig. 4(b) shows the radiation pattern in which the electric dipole is dominant. The resulting radiation pattern is bidirectional; similar behavior can be observed in the case of a dominant magnetic dipole mode [35]. This illustrates that the electric and magnetic dipoles must be superimposed orthogonally and in correct proportion to achieve a unidirectional antenna pattern.

It should further be emphasized that this Huygens' source perspective distinguishes the GSP resonators from
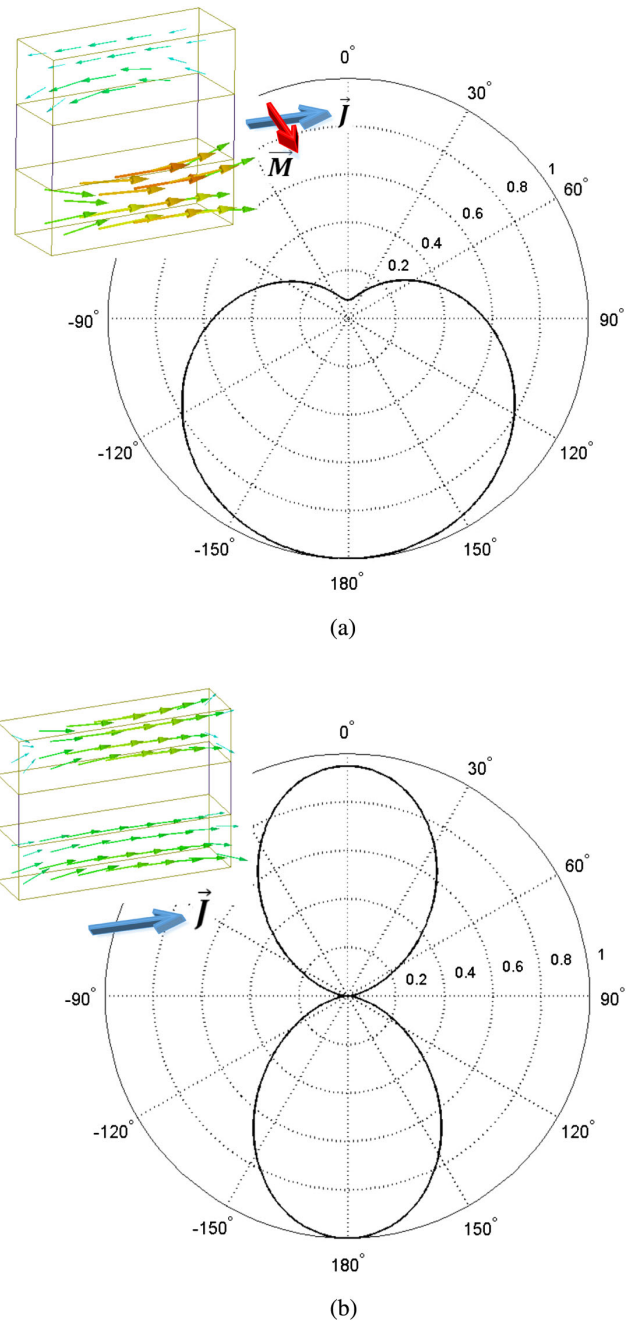
FIG. 4. Radiation pattern of a single isolated unit cell (a) when the GSP resonator simultaneously excites orthogonal electric and magnetic dipoles and (b) when the electric dipole is dominant. The insets show the induced current distribution upon normal plane-wave incidence at $\lambda = 800$ nm. The dimensions of the two gold nanorods and silica spacer are (a) 50 nm × 50 nm × 140 nm and (b) 50 nm × 50 nm × 200 nm. Blue ($\vec{J}$) and red ($\vec{M}$) arrows indicate the directions of induced electric and magnetic currents, respectively.

other seemingly similar structures such as the V-shaped antennas [6] and rotated single-layer nanorods [10,36,37]. These structures may provide a small magnetic dipole moment that is perpendicular to the metasurface plane, but
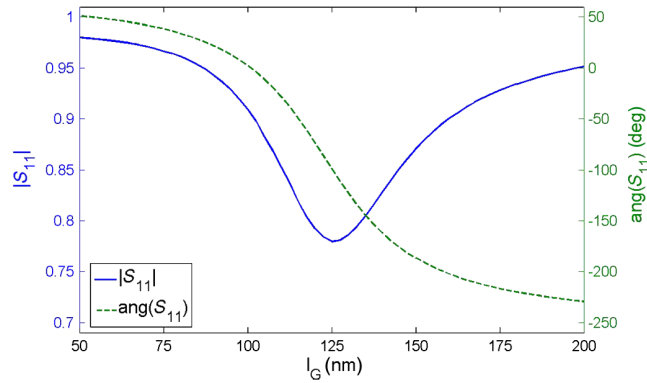
FIG. 5. S_{11} (reflection coefficient) of an infinite array of GSP resonators as a function of their lengths.

FIG. 6.   The transformed magnitudes (blue line) and phases (green line) of the S_{11} parameters from the equivalent circuit.

their operation as metasurfaces rely mainly on their electric responses. As a result, the phase response of individual unit cells for these devices spans 180° at most. Moreover, because of the absence of magnetic responses, when metasurfaces with such unit cells are utilized to arbitrarily refract or reflect incident fields, other spurious plane waves are excited along with the main beam, as examined in Ref. [15]. On the other hand, GSP resonators support both electric and magnetic currents, which combine to minimize the excitation of unwanted plane waves. The suppression is seen if the electric and magnetic surfaces are separately examined [15]. Furthermore, orthogonal electric and magnetic dipoles combine to allow a full-phase tuning range of 360°. This can be understood from a Huygens' source's equivalent circuit model which has been shown to be a so-called lattice network [20], the topology of which is shown next to the unit cell in Fig. 3. The lattice network is frequently used in all-pass filter designs where the main goal is to control the relative phase difference between the input and output ports from 0° to 360° [38]. A similar phase control can be observed at optical frequencies. This is shown in Fig. 5, where the reflective response of the surface is obtained for different lengths of a nanorod GSP resonator. It is seen that the magnitude of the reflection coefficient, $|S_{11}|$, is close to unity, while its phase ranges from 50° to −230°; a significant increase compared to the single resonance that covers 180° at most. The dip in magnitude that coincides with a rapid phase transition is due to Ohmic loss and can be made small at the cost of reduced phase control [21]. In the next section, we will show how to also control the magnitude response.

The series and shunt impedances of Z_1 and Z_2 in lattice networks, shown in Fig. 3, are respectively related to the induced magnetic and electric currents, through the conditions $Z_1 = Z_s^m/2$ and $Z_2 = 2Z_s^e$, which arise by comparing the electromagnetic boundary condition with its circuit equivalent [20]. Therefore, the required complex impedances can be conveniently transformed to the scattering parameters, as shown in Fig. 6 (see Appendix A), where S_{11} and S_{21} denote reflection and transmission coefficients
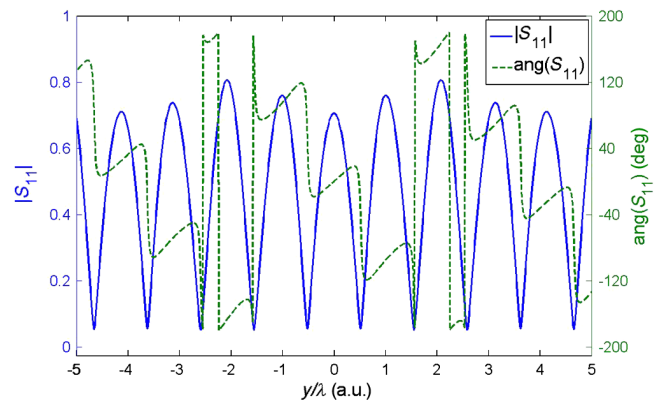
respectively. We note that the method outlined in Refs. [14,23] is also capable of relating impedances to reflection and transmission coefficients and is in agreement with the one employed here. Finally, we note that only S_{11} parameters are shown here. The required S_{21} parameters are small because we have initially stipulated the transmitted field to be negligible. This condition also corresponds to the actual S_{21} parameters of the GSP resonators because of their dominant reflective property. Thus, the complex-valued surface impedance can be realized by encoding only the equivalent S_{11} values on the nanorod GSP resonators.

B. Independent control of the magnitude and phase of the local reflection coefficients

The equivalent S_{11} parameters that satisfy the boundary conditions across the surface show that one must be able to independently control the magnitudes and phases of S_{11}. Whereas the previous section has shown that one can tailor the reflection phase of our proposed Huygens' metasurface by varying the length of the nanorod, we hereby introduce an extra degree of freedom by also rotating individual nanorods at an angle θ, as shown in Fig. 3, to control the magnitude. This allows decoupling of the fixed relationship between the phases and magnitudes of S_{11}. The angle θ is defined as the angle between the axis where a nanorod varies its length (resonator axis) and the polarization direction of the incident electric field, as shown in Fig. 3. Following the coordinate convention in Fig. 3, we set the y axis as our resonator axis and define r_x and r_y as the reflection coefficients of the surface in the case of plane-wave excitations that are linearly polarized along the x and y directions, respectively. r_x and r_y can be numerically obtained for different lengths of the GSP resonator, and an analytical expression for the reflected field $\vec{E}_{ref}$ can be given for $\theta \neq 0°$ in the case of y-polarized plane-wave input, $\vec{E}_{in} = E_{oy}\vec{a}_y e^{j\beta z}$, through the change of coordinate system as
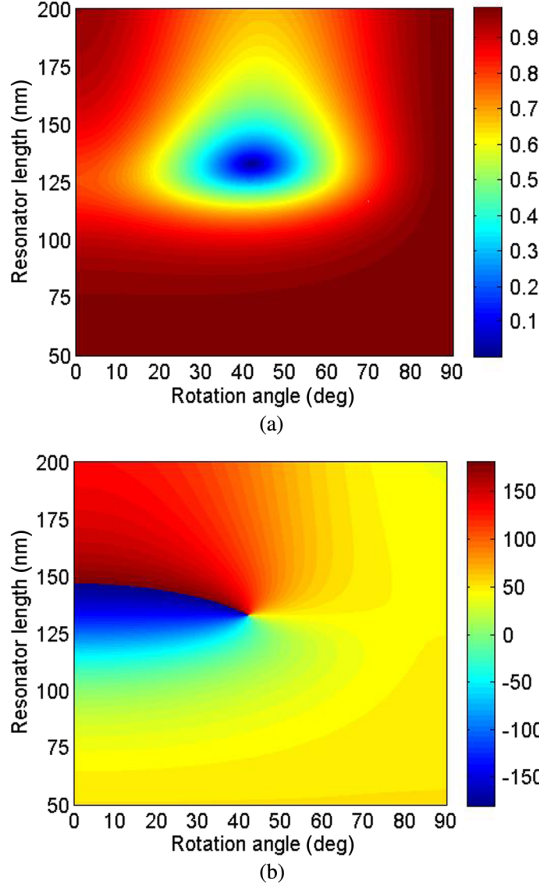
(a)

(b)

FIG. 7. Variation in (a) magnitude and (b) phase of S_{11} in degrees for different resonator lengths and rotation angles.

$$\vec{\mathbf{E}}_{\mathrm{ref}} = E_{\mathrm{oy}}[\cos\theta\sin\theta(r_x - r_y)\vec{\mathbf{a}}_x$$
$$+ (r_x\sin^2\theta + r_y\cos^2\theta)\vec{\mathbf{a}}_y]e^{-j\beta z}. \quad (3)$$

Equation (3) predicts the reflected field for various lengths and rotation angles of the resonator. The reflected field as a function of different resonator lengths is fully numerical since r_x and r_y are from full-wave simulation. However, the reflected field as a function of rotation angle is obtained analytically; hence, the overall expression is seminumerical. Nevertheless, it shows great accuracy compared to the full-wave simulation result (see Appendix B), and it offers a quick way to relate lengths and rotation angles of the resonator to specific reflection coefficients. The resulting reflection coefficient $S_{11} = \vec{\mathbf{E}}_{\mathrm{ref}} \cdot \vec{\mathbf{a}}_y/E_{\mathrm{oy}}$, as a function of the rotation angle θ and the length of the GSP resonators, l_G, is shown in Fig. 7. To further clarify the accessible range of the reflection coefficients, Fig. 8 shows the available range in the Cartesian and polar coordinate systems. As already seen, nearly arbitrary control of the complex reflection coefficient is feasible. We note that one can completely control the phase from 0° to 360° if the magnitude is normalized by 67.25%. In other words, one can realize *any* combination of complex reflection coefficient with magnitude and phase
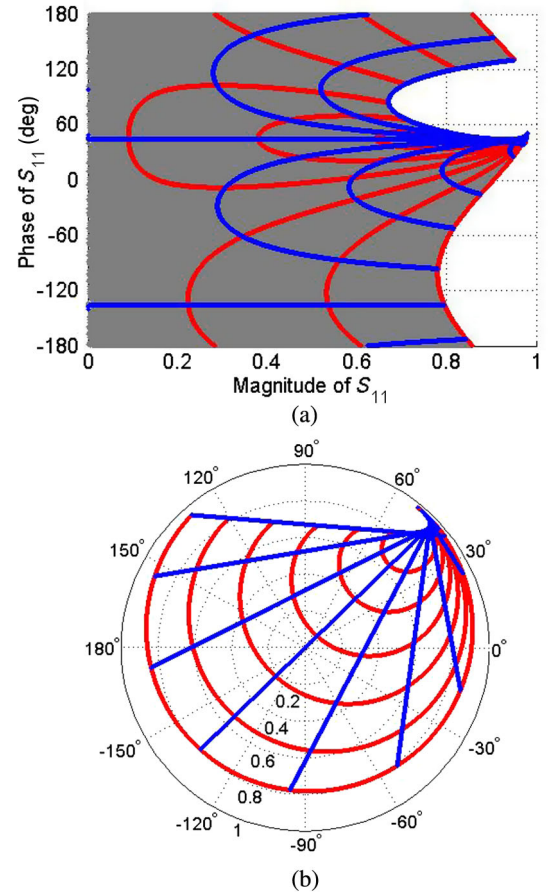

(a)

(b)

FIG. 8. Accessible range of complex reflection coefficients. (a) A magnitude vs phase plot showing the range of achievable S_{11} values with the proposed optical Huygens' metasurface. The achievable values are shaded in gray; varying the rod length and rotation angle corresponds to traveling along the red and blue contours, respectively. (b) The same plot shown with the magnitude and phase of S_{11} plotted in polar coordinates. As in (a), varying the rod length and rotation angle corresponds to traveling along the red and blue contours, respectively.

ranging from 0 to 0.6725 and 0° to 360°, respectively. At the cost of reduced phase control, the efficiency of the surface can be enhanced. In other words, one can realize a complex reflection coefficient with magnitude and phase ranging from 0 to 0.8 and 50° to −230°, respectively.

Equation (3) shows that cross-polarized components are induced for $\theta > 0$. Such cross-polarized components should not be confused with the ones found in structures such as the V-shaped nanoantennas, where the cross-polarized components are always present and fundamentally limit the efficiency to 25% even in the lossless case [11]. In our design, however, cross-polarized components are induced only when the resonator is rotated to independently control the magnitude and phase of the reflection coefficient. If the magnitude of the reflection coefficient is to be maximized (which most previous works have attempted to achieve), then the cross-polarized components
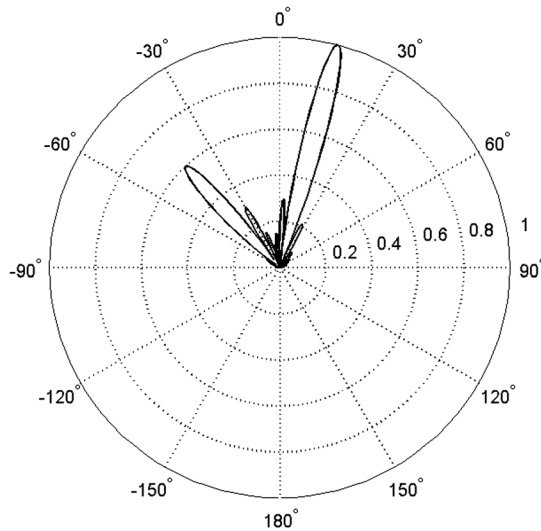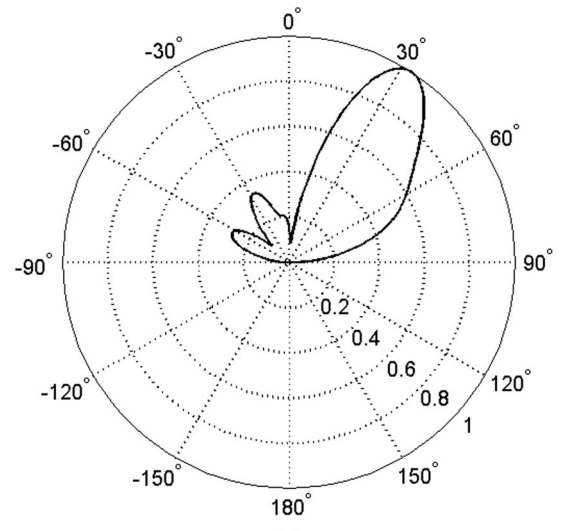
FIG. 9.   Far-field plot of the beam splitter with 25 unit cells.

(a)

(b)

FIG. 10.   Radiation patterns of (a) Dolph-Tschebyscheff and (b) uniform arrays. Both arrays redirect the normally incident plane wave at 33°.

are not induced. From the pool of available S_{11} parameters, the required spatially dependent S_{11} values for the beam splitter are sampled for 25 data points, and its full-wave simulation result is shown in Fig. 9 (see Appendix B). A distinct asymmetric splitting effect is observed at prescribed angles, which proves that the proposed physical implementation method closely approximates the desired complex surface impedances. The difference in the amplitudes of the two reflected beams arises from the fact that each unit cell has a near-cardioid radiation pattern where the intensity reduces away from broadside. This can be compensated by assigning a higher amplitude for the field which reflects further from the broadside. For the current beam splitter, we note that infinitely many unit cells are needed to exactly simulate aperiodic impedance profiles, as periodic boundary condition cannot be employed.

III. EXTENSION TO OPTICAL REFLECTARRAY THEORY: DOLPH-TSCHEBYSCHEFF PATTERN

The ability to independently control the magnitudes and phases of the complex reflection coefficients greatly aids the design of specialized optical reflectarrays. Most previous metasurface designs, which aim to arbitrarily reflect or refract incident fields, can be viewed as reflectarrays or transmitarrays. In these designs, constant scattering amplitudes are assumed for all unit cells with a linear phase progression [6,10,11,29]. From the antenna-theory perspective, such distributions are analogous to uniform antenna arrays which provide radiation patterns with the maximum radiation directed at a designed angle. However, it is well known that uniform arrays also result in uncontrolled and uneven sidelobes. In contrast, the method proposed in this paper allows the realization of limitless optical antenna patterns, including ones that feature constant and minimized sidelobe levels (SLLs). As a
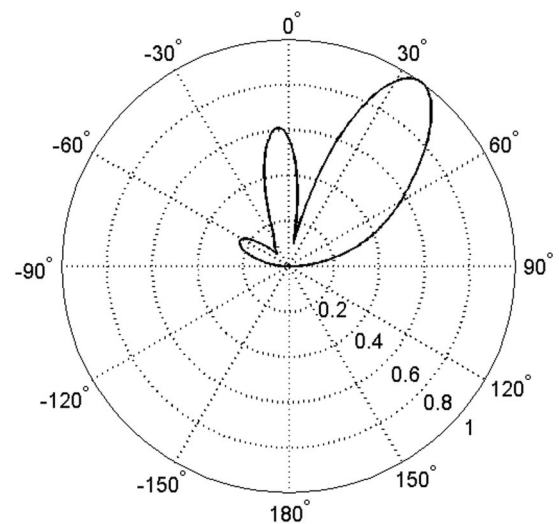
demonstration, we present an optical Dolph-Tschebyscheff reflectarray to precisely tailor the SLLs.

In Dolph-Tschebyscheff reflectarrays, the reflection coefficient of each unit cell is weighted by the mth order Tschebyscheff polynomial $T_m(z)$, where the number of unit cells forming the array is $m + 1$. An interesting property of the Tschebyscheff polynomials is that they assume values from -1 to 1 within the range $-1 \leq z \leq 1$, where all the roots occur. Using this property, antenna arrays designed through a mapping from the Tschebyscheff function feature array factors with constant ripple sidelobes. This enables one to achieve the lowest possible SLL given a specific beam angle and beamwidth. In this work, we use an optical Huygens' metasurface to synthesize a Dolph-Tschebyscheff array. Assuming five isotropic elements, the array is designed to radiate at 56.5° from the broadside
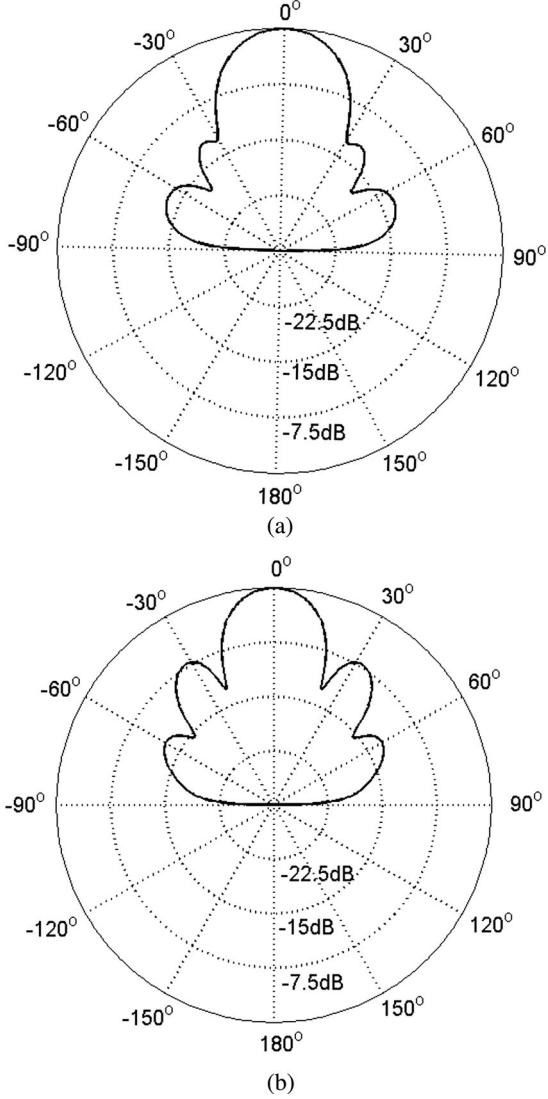
(a)

(b)

FIG. 11. Radiation patterns of (a) Dolph-Tschebyscheff and (b) uniform arrays. Both arrays normally reflect the incident plane wave.

TABLE I. Normalized reflection coefficients of each unit cell in a five-element Dolph-Tschebyscheff reflectarray. The resulting array factor directs its main beam at 56.5° provided that each element radiates isotropically. l_G and θ represent the length and the rotated angle, respectively, of each GSP resonator that correspond to the desired S_{11}.

Unit cell	$|S_{11}|$	$\text{ang}(S_{11})$	l_G [nm]	θ
#1	0.518	180°	140	35°
#2	0.833	90°	162.5	45°
#3	1.0	0°	115	45°
#4	0.833	−90°	125	25°
#5	0.518	−180°	140	35°

TABLE II. Normalized reflection coefficients of each unit cell in a five-element Dolph-Tschebyscheff reflectarray that reflects a normally incident plane wave at its broadside.

Unit cell	$|S_{11}|$	$\text{ang}(S_{11})$	l_G (nm)	θ
#1	0.518	0°	128	36°
#2	0.833	0°	123	27°
#3	1.0	0°	120	0°
#4	0.833	0°	123	27°
#5	0.518	0°	128	36°

size of five unit cells, which amounts to 1.2 μm. Much tighter beams can be synthesized with larger antennas. To further demonstrate sidelobe suppression, Figs. 11(a) and 11(b) compare broadside radiation patterns in the dB scale (normal incidence and reflection), where the distribution of the reflection coefficients of each unit cell is summarized in Table II. In this design, the Dolph-Tschebyscheff array results in a slightly wider beamwidth, but much lower SLLs are obtained as compared to those of the uniform array. Furthermore, the peaks of the sidelobes are of equal amplitudes.

IV. CONCLUSION

We have presented the optical Huygens' metasurface—a metasurface that can independently and widely control the magnitude and phase of its local reflection coefficients. This has been achieved using nanorod resonators to synthesize Huygens' sources that excite orthogonal electric and magnetic dipoles. The proposed physical dimensions of the nanorod GSP resonators fall under practical electron-beam resolution. Moreover, similar structures, but for different functionalities, have been successfully fabricated in the past, proving the feasibility and versatility of the proposed optical Huygens' metasurfaces [29,40]. By rotating these resonators and altering their lengths, such metasurfaces with tailored reflection coefficients can be synthesized. The idea of generalized complex reflection coefficients extends beyond the realization of general-purpose metasurfaces and opens pathways towards many

(z axis). Table I summarizes the distribution of (normalized) reflection coefficients of the array that are weighted based on $T_4(z)$, and Fig. 10(a) shows the resulting total radiation pattern. The details of the design process for a Dolph-Tschebyscheff array are outlined in Ref. [39]. As shown, the peaks of the two sidelobes in the radiation pattern are nearly constant, while the uniform array possesses uneven and significant sidelobes [Fig. 10(b)]. We note that the presented radiation pattern is the total radiation pattern (product of unit-cell and Dolph-Tschebyscheff array patterns). As such, the main beam is directed at 33°, instead of 56.5°, which we designed for the array pattern, since the intensity of the unit-cell pattern decreases away from the broadside, as shown in Fig. 4(a). Moreover, the main beams obtained are already quite directive, considering that the antennas have a small overall

designs of unique optical reflectarrays such as the Dolph-Tschebyscheff array, featuring equal-amplitude sidelobes of prescribed magnitude, as demonstrated in this paper. The independent control over the magnitudes and phases of complex reflection coefficients brings extreme flexibility in reshaping an optical wavefront. This allows the realization of a myriad of optical antenna patterns including binomial and superdirective patterns.

ACKNOWLEDGMENTS

APPENDIX A: TRANSFORMATION FROM COMPLEX IMPEDANCES TO REFLECTION COEFFICIENTS

The reflection coefficient Γ (or S_{11}) of the lattice network shown in Fig. 3 can be solved as

$$\Gamma = \frac{\tilde{Z}_1 - \tilde{Z}_2}{\tilde{Z}_1 + \tilde{Z}_2}, \tag{A1}$$

where

$$\begin{aligned}\tilde{Z}_1 &= Z_1(Z_{o2} + Z_2) + Z_2(Z_{o2} + Z_1) \\ \tilde{Z}_2 &= Z_{o1}(2Z_{o2} + Z_1 + Z_2).\end{aligned} \tag{A2}$$

Here, Z_1 and Z_2 respectively correspond to $Z_S^m/2$ and $2Z_S^e$, which result from comparing the electromagnetic boundary condition with the port relationship in the lattice network [20]. Z_{o1} and Z_{o2} are the characteristic impedances (η) of media 1 and 2 separated by the metasurface. In our simulations, we have assumed that the two are of the same media ($Z_{o1} = Z_{o2} = 377\,\Omega$—the intrinsic impedance of free space). Setting Z_{o2} as an impedance of air, not as an impedance of gold, implies that we are interpreting the whole structure as a single-layered surface. It is assumed that a plane-wave excitation is from medium 1. If the transmitted field is also to be arbitrarily refracted at some angle (θ_t) (a case we did not consider in this paper), then $Z_{o2} = \eta \cos\theta_t$ (for TM polarizations) or $Z_{o2} = \eta \sec\theta_t$ (for TE polarizations).

APPENDIX B: NUMERICAL SIMULATION

Full-wave electromagnetic simulations are performed using the Ansoft HFSS Finite Element Method commercial software. The Drude model in Ref. [41] is used to obtain the optical properties of gold. A constant refractive index of 1.45 is used for the silica layer. A nanorod GSP resonator unit cell is characterized by surrounding its four sides with a periodic boundary condition and terminating the top and
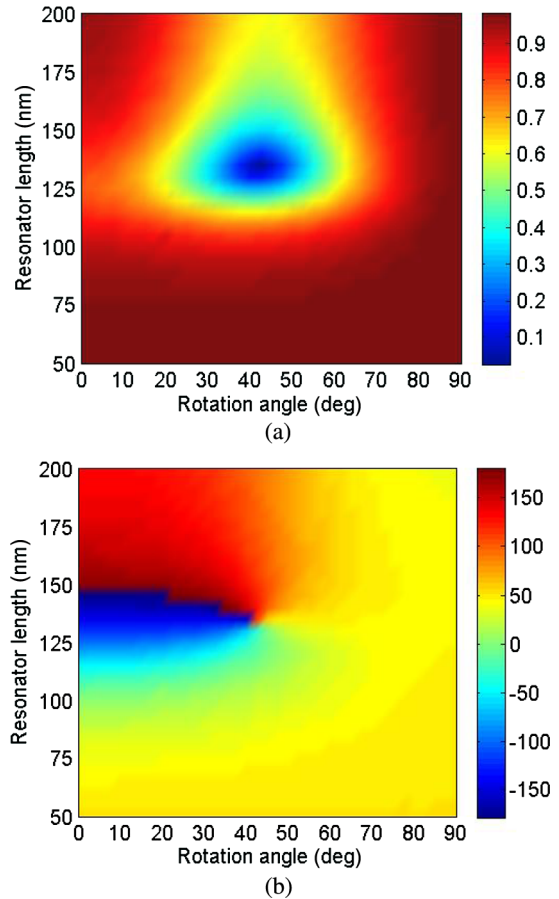

(a)

(b)

FIG. 12. Full-wave unit-cell characterization result: variations in (a) magnitude and (b) phase of S_{11} for different resonator lengths and rotation angles.

bottom faces with Floquet ports for a normally incident plane-wave excitation. The electric and magnetic surface impedances can be directly extracted from the impedance parameters that HFSS computes as follows:

$$\begin{aligned} Z_s^e &= \frac{(Z_{11} + Z_{21})}{2} \\ Z_s^m &= 2Z_{11}Z_{21} \\ Z_{ij} &= \left.\frac{V_i}{I_j}\right|_{V_k=0 \quad \text{for } k \neq j}, \end{aligned} \tag{B1}$$

where the subscripts i and j represent the top and bottom Floquet ports, respectively. For all simulations, w, t_1, and t_2 (refer to Fig. 3) are all fixed to 50 nm, while the resonator's length l_G and the rotation angle θ vary from 50 nm–200 nm and 0°–90°, respectively, depending on the desired reflection coefficient. For all simulations except for Figs. 11(a) and 11(b), the periodicities in the x and y directions are fixed to $d_x = 240$ nm and $d_y = 240$ nm. Figure 12 shows the full-wave unit-cell characterization result based on the above physical geometries, which closely matches Fig. 7. The unit-cell periodicities used for Figs. 11(a) and 11(b) are

changed to $d_x = 400$ nm and $d_y = 400$ nm, in order to increase the number of sidelobes from 1 to 2 for better visualization of equal peak amplitudes. The radiation patterns of the beam splitter and optical reflectarrays are obtained by simulating 25×1 and 5×1 unit cells, respectively. The whole structure is surrounded by the radiation boundary condition except for those faces that are normal to the direction where the reflection coefficient does not vary. These faces are terminated by the periodic boundary condition (x axis in Fig. 1).

---

[1] J. Goodman, *Introduction to Fourier Optics*, 3rd ed. (Roberts and Company, Englewood, Colorado, 2004).

[2] B. Walther, C. Helgert, C. Rockstuhl, and T. Pertsch, *Diffractive Optical Elements Based on Plasmonic Metamaterials*, Appl. Phys. Lett. **98**, 191101 (2011).

[3] B. Walther, C. Helgert, C. Rockstuhl, F. Setzpfandt, F. Eilenberger, E. Kley, F. Lederer, A. Tünnermann, and T. Pertsch, *Spatial and Spectral Light Shaping with Metamaterials*, Adv. Mater. **24**, 6300 (2012).

[4] P. F. Checcacci, V. Russo, and A. M. Scheggi, *Holographic Antennas*, IEEE Trans. Antennas Propag. **18**, 811 (1970).

[5] K. Iizuka, M. Mizusawa, S. Urasaki, and H. Ushigome, *Volume-Type Holographic Antenna*, IEEE Trans. Antennas Propag. **23**, 807 (1975).

[6] N. Yu, P. Genevet, M. A. Kats, F. Aieta, J. Tetienne, F. Capasso, and Z. Gaburro, *Light Propagation with Phase Discontinuities: Generalized Laws of Reflection and Refraction*, Science **334**, 333 (2011).

[7] N. Yu, F. Aieta, P. Genevet, M. A. Kats, Z. Gaburro, and F. Capasso, *A Broadband, Background-Free Quarter-Wave Plate Based on Plasmonic Metasurfaces*, Nano Lett. **12**, 6328 (2012).

[8] N. Yu, P. Genevet, F. Aieta, M. A. Kats, R. Blanchard, G. Aoust, J. Tetienne, Z. Gaburro, and F. Capasso, *Flat Optics: Controlling Wavefronts with Optical Antenna Metasurfaces*, IEEE J. Sel. Top. Quantum Electron. **19**, 4700423 (2013).

[9] X. Ni, N. K. Emani, A. V. Kildishev, A. Boltasseva, and V. M. Shalaev, *Broadband Light Bending with Plasmonic Nanoantennas*, Science **335**, 427 (2012).

[10] X. Ni, A. V. Kildishev, and V. M. Shalaev, *Metasurface Holograms for Visible Light*, Nat. Commun. **4**, 2807 (2013).

[11] F. Monticone, N. M. Estakhri, and A. Alù, *Full Control of Nanoscale Optical Transmission with a Composite Metascreen*, Phys. Rev. Lett. **110**, 203903 (2013).

[12] Z. Bomzon, G. Biener, V. Kleiner, and E. Hasman, *Space-Variant Pancharatnam-Berry Phase Optical Elements with Computer-Generated Subwavelength Gratings*, Opt. Lett. **27**, 1141 (2002).

[13] D. Lin, P. Fan, E. Hasman, and M. L. Brongersma, *Dielectric Gradient Metasurface Optical Elements*, Science **345**, 298 (2014).

[14] C. Pfeiffer and A. Grbic, *Metamaterial Huygens' Surfaces: Tailoring Wave Fronts with Reflectionless Sheets*, Phys. Rev. Lett. **110**, 197401 (2013).

[15] M. Selvanayagam and G. V. Eleftheriades, *Discontinuous Electromagnetic Fields Using Orthogonal Electric and Magnetic Currents for Wavefront Manipulation*, Opt. Express **21**, 14409 (2013).

[16] J. Wong, M. Selvanayagam, and G. V. Eleftheriades, A Thin Printed Metasurface for Microwave Refraction, in *IEEE International Microwave Symposium* (IEEE, 2011).

[17] Y. Zhao, M. A. Belkin, and A. Alù, *Twisted Optical Metamaterials for Planarized Ultrathin Broadband Circular Polarizers*, Nat. Commun. **3**, 870 (2012).

[18] C. Pfeiffer, N. K. Emani, M. K. Shaltout, A. Boltasseva, V. M. Shalaev, and A. Grbic, *Efficient Light Bending with Isotropic Metamaterial Huygens' Surfaces*, Nano Lett. **14**, 2491 (2014).

[19] N. M. Estakhri and A. Alù, *Manipulating Optical Reflections Using Engineered Nanoscale Metasurfaces*, Phys. Rev. B **89**, 235419 (2014).

[20] M. Selvanayagam and G. V. Eleftheriades, *Circuit Modeling of Huygens Surfaces*, IEEE Antennas Wireless Propag. Lett. **12**, 1642 (2013).

[21] A. Pors and S. I. Bozhevolnyi, *Plasmonic Metasurfaces for Efficient Phase Control in Reflection*, Opt. Express **21**, 27438 (2013).

[22] E. F. Kuester, M. A. Mohamed, M. Piket-May, and C. L. Holloway, *Averaged Transition Conditions for Electromagnetic*, IEEE Trans. Antennas Propag. **51**, 2641 (2003).

[23] C. L. Holloway, M. A. Mohamed, E. F. Kuester, and A. Dienstfrey, *Reflection and Transmission Properties of a Metafilm: With an Application to Controllable Surface Composed of Resonant Particles*, IEEE Transactions on Electromagnetic Compatibility **47**, 853 (2005).

[24] W. R. Holland and D. G. Hall, *Frequency Shifts of an Electric-Dipole Resonance Near a Conducting Surface*, Phys. Rev. Lett. **52**, 1041 (1984).

[25] J. Cesario, M. U. Gonzalez, S. Cheylan, W. L. Barnes, S. Enoch, and R. Quidant, *Coupling Localized and Extended Plasmons to Improve the Light Extraction through Metal Films*, Opt. Express **15**, 10533 (2007).

[26] Y. Chu, M. G. Banaee, and K. B. Crozier, *Double-Resonance Plasmon Substrates for Surface-Enhanced Raman Scattering with Enhancement at Excitation and Stokes Frequencies*, ACS Nano **4**, 2804 (2010).

[27] Y. Chu, D. Wang, W. Zhu, and K. B. Crozier, *Double Resonance Surface Enhanced Raman Scattering Substrates: An Intuitive Coupled Oscillator Model*, Opt. Express **19**, 14919 (2011).

[28] V. M. Shalaev, W. Cai, U. K. Chettiar, H. Yuan, A. K. Sarychev, V. P. Drachev, and A. V. Kildishev, *Negative Index of Refraction in Optical Metamaterials*, Opt. Lett. **30**, 3356 (2005).

[29] S. Sun, K. Yang, C. Wang, T. Juan, W. T. Chen, C. Y. Liao, Q. He, S. Xiao, W. Kung, G. Guo, L. Zhou, and D. P. Tsai, *High-Efficiency Broadband Anomalous Reflection by Gradient Meta-surfaces*, Nano Lett. **12**, 6223 (2012).

[30] A. Pors and S. I. Bozhevolnyi, *Efficient and Broadband Quarter-Wave Plates by Gap-Plasmon Resonators*, Opt. Express **21**, 2942 (2013).

[31] C. Huygens, *Traité de la Lumieére* (Pieter van der aa, Leyden, 1690).

[32] D. M. Pozar, New Results for Minimum Q, Maximum Gain, and Polarization Properties of Electrically Small Arbitrary Antennas, in *3rd European Conference on Antennas and Propagation, EuCAP 2009* (IEEE, 2009), pp. 1993–1996.

[33] T. Niemi, P. Alitalo, A. O. Karilainen, and S. A. Tretyakov, *Electrically Small Huygens Source Antenna for Linear Polarisation*, IET Microwaves Antennas Prop. **6**, 735 (2012).

[34] M. J. Underhill and M. J. Blewett, Undirectional Tuned Loop Antennas Using Combined Loop and Dipole Modes, in *Eighth International Conference on HF Radio Systems and Techniques, 2000 (IEE Conf. Publ. No. 474)*, (IET, 2000), pp. 37–41.

[35] J. Peng and R. W. Ziolkowski, *Metamaterial-Inspired, Electrically Small Huygens Sources*, Antennas Wireless Propag. Lett., IEEE **9**, 501 (2010).

[36] X. Chen, L. Huang, H. Mühlenbernd, G. Li, B. Bai, Q. Tan, G. Jin, C. Qiu, S. Zhang, and T. Zentgraf, *Dual-Polarity Plasmonic Metalens for Visible Light*, Nat. Commun. **3**, 1198 (2012).

[37] L. Huang, X. Chen, H. Mühlenbernd, H. Zhang, S. Chen, B. Bai, Q. Tan, G. Jin, K. Cheah, C. Qiu, J. Li, T. Zentgraf, and S. Zhang, *Three-Dimensional Optical Holography Using a Plasmonic Metasurface*, Nat. Commun. **4**, 2808 (2013).

[38] R. Schaumann and V. V. Mac, *Design of Analog Filters*, 2nd ed. (Oxford University Press, New York, 2001).

[39] C. A. Balanis, *Antenna Theory: Analysis and Design*, 3rd ed. (Wiley-Interscience, New York, 2005).

[40] A. Pors, O. Albrektsen, I. P. Radko, and S. I. Bozhevolnyi, *Gap Plasmon-Based Metasurfaces for Total Control of Reflected Light*, Sci. Rep. **3**, 2155 (2013).

[41] P. G. Etchegoin, E. C. Le Ru, and M. Meyer, *An Analytic Model for the Optical Properties of Gold*, J. Chem. Phys. **125**, 164705 (2006).